

# Advanced Integration of a Switched-Coupled-Inductor Ćuk Converter for Optimized Grid-Connected PV Application

Farid Oufqir <sup>1</sup>, Mohamed Bendaoud <sup>2</sup>, Fatima Ezzahra Tahiri <sup>3</sup>, and Khalid Chikh <sup>4</sup>

<sup>1,2,4</sup> Sultan Moulay Slimane University, National School of Applied Sciences, Khouribga, Morocco

<sup>3</sup> Hassan II University, National Higher School of Electricity and Mechanics, Casablanca, Morocco

farid.oufqir@usms.ac.ma, m.bendaoud@usms.ma, fatima-ezzahra.tahiri@ensem.ma, k.chikh@usms.ma

## ABSTRACT

Advanced converters offer superior performance over traditional models by increasing converter efficiency. However, there is a significant gap in integrating these advanced converters into grid-connected photovoltaic (GCPV) systems. This paper addresses this gap by presenting the integration of a novel Ćuk converter that combines a switched inductor (SL) with coupled inductors (CI) in a two-stage, three-phase GCPV system. The proposed system also incorporates an LCL filter to reduce harmonic distortion, while active and reactive power (PQ) control effectively manages power using a three-phase inverter. Virtual experiments were performed in MATLAB/Simulink® to evaluate the performance of the novel converter within the PV system. These simulations assessed the efficiency of the hybrid Ćuk converter compared to conventional converters while also analyzing the impact of the turns ratio on overall system performance. The results demonstrated significant improvements in both efficiency and power quality. This study contributes to the renewable energy field by providing an analysis of advanced DC-DC converter integration, offering an optimized solution for GCPV systems.

**Index-words:** Ćuk converter, Coupled Inductors, Switched inductor, Grid-Connected System.

## I. INTRODUCTION

In PV systems, the efficient extraction and conversion of solar energy into electrical power are critical for optimal performance. Single-stage PV systems have been employed, where maximum power point tracking (MPPT) and DC-AC conversion are integrated into a single process. This approach offers simplicity and cost savings due to fewer components [1].

However, single-stage systems often suffer from significant voltage oscillations, which can reduce the efficiency of MPPT and degrade power quality. The inherent coupling of functions makes it challenging to optimize both power extraction and conversion simultaneously. In two-stage PV systems, the functions are separated into distinct stages: a DC-DC converter stage that optimizes power extraction from the PV array and an inverter stage that converts the optimized DC voltage into AC power suitable for grid connection [2]. This separation enables independent optimization of each stage, leading to higher overall efficiency and improved

power quality. Two-stage systems can employ advanced control strategies, such as dual closed-loop control. These strategies include feedforwarding the grid voltage and using PI or proportional-resonant controllers to finely regulate the inverter output current based on reference signals derived from the grid voltage [3][4]. Grid-connected inverters must synchronize their output with the grid voltage in terms of frequency, phase, and amplitude to facilitate seamless power injection [5]. Advanced control strategies are employed to achieve this synchronization while maintaining power quality and complying with grid codes and standards.

Moreover, the inverter control system must address challenges such as harmonic distortion, reactive power compensation, and the ability to ride through grid disturbances like voltage sags or frequency deviations. Different techniques have been developed to enhance the dynamic response and robustness of the inverter under varying grid conditions [6]. The integration of grid-connected inverters also necessitates compliance with stringent grid codes, which dictate requirements

for power quality, fault ride-through capabilities, and the provision of ancillary services such as frequency and voltage support [7]. Therefore, the design of inverter control strategies must not only focus on optimal power transfer but also on fulfilling regulatory standards and adapting to dynamic grid environments.

The choice of a DC-DC converter in the first stage is crucial for the performance of two-stage PV systems. Traditional converters are commonly used for MPPT and voltage regulation. However, these converters have inherent limitations. Buck converters are restricted to step-down operations, limiting their applicability in systems requiring voltage boost. Boost converters can step up the voltage but often struggle with high input current ripple and electromagnetic interference, leading to reduced efficiency and increased stress on components. Buck-boost converters offer bidirectional conversion but may exhibit lower efficiency due to high switching and conduction losses. To overcome these challenges, several advanced DC-DC converter topologies have been proposed to enhance voltage gain, reduce input ripple, and minimize electromagnetic interference [8]. One such method is the Voltage Multiplier Cell (VMC) technique, which integrates VMCs with basic step-up converters to significantly increase voltage gain, making it suitable for applications requiring high output voltage from low voltage [9].

However, the use of multiple components increases hardware complexity and cost, and maintaining good voltage regulation can be challenging. Another advanced method is the use of Coupled Inductor (CI) topologies. CI leverages the energy storage capabilities of inductors during each switching period to achieve higher voltage gains. By adjusting the turns ratio of the coupled inductor, significant voltage amplification can be realized. CI techniques are popular for their ability to handle high power and provide good voltage regulation.

The Voltage Lift (VL) technique is also highlighted for its simplicity and effectiveness in boosting output voltage. This method involves charging capacitors to specific voltage levels sourced from the input voltage and then using these charged capacitors to achieve higher output voltages. The VL technique can be combined with other advanced topologies, such as quadratic boost converters, to further enhance voltage gain and reduce voltage stress on components. Switched Inductor (SL) [10] and Switched Capacitor (SC) techniques are methods that leverage the energy storage capabilities of inductors and capacitors to achieve higher voltage gains and improve voltage regulation. Cascaded topologies involve the connection of multiple converter stages in series to achieve exponential voltage gains [11]. It is effective for medium to high-power applications.

TABLE I. VARIOUS DC-DC CONVERTERS TOPOLOGIES AND THEIR APPLICATIONS

DC-DC Converter & Techniques	Configuration	Key Results
VL-SL Multilevel Boost Converter [10]	Standalone DC-DC converter with resistive load	Efficiency over 90%, Output voltage 95.5V from 12V input, 50 kHz switching frequency
Multilevel Boost Converter with CI [11]	Standalone DC-DC converter with resistive load	Efficiency around 92%, Output voltage 90V from 20V input, 100 kHz switching frequency
Quadratic boost converter with VL Technique [12]	Standalone DC-DC converter with resistive load	Efficiency over 96.6%, Output voltage 250V from 18V input, 40 kHz switching frequency
Ćuk and Boost Using Single Switch [13]	Standalone DC-DC converter with resistive load	Efficiency 92.2%, Output voltage 122V from 24V input, 50 kHz switching frequency
POSLC converter with PI Resonant Controller [14]	1Ø Two-stage Grid-connected	Efficiency 97.5%, Voltage gain higher than boost converter
Symmetrical VMC Interleaved boost Converter [15]	Standalone DC-DC converter with resistive load	Efficiency 96%, Voltage gain of 16, Output voltage 400V from 25V input
VMC Based Quasi-Switched Boost Inverter [16]	3Ø Two-stage Grid-connected	Efficiency 91.3%, Output voltage 181V from 50V input, THD 0.9%

CI quadratic Converter [17]	Standalone DC-DC converter with resistive load	Efficiency 96.9%, Output voltage 380V from 48V input, 500W power output
Dual-Switch CI Based High Step-Up Converter [18]	Standalone DC-DC converter resistive load	Efficiency 95.6%, Voltage gain of 20, Output voltage 400V from 20V input
Conventional SEPIC Converter [19]	3Ø Two-stage Grid-connected	Efficiency around 97%, Total Harmonic Distortion (THD) 0.65%, DC-link reference voltage 600V
POSCLC with Hybrid Switching Capacitor-Inductor Cell [20]	Standalone DC-DC converter with resistive load	Efficiency over 95%, Voltage gain 8x at duty cycle 0.5, 20x at duty cycle 0.8, Output voltage ripple 0.004V
Interleaved Converter with Winding Cross CI-VMC [21]	Standalone DC-DC converter with resistive load	Gain 12.5, Efficiency 96%, Current ripple 3.6A, Voltage stress on switches 80V
Converter with CI-SC Techniques [22]	Standalone DC-DC converter with resistive load	Efficiency 96%, Voltage gain 20, Input current ripple 1.8A, Voltage stress on switches 120V
VL Cell Split source Inverter (SSI) [23]	3Ø single-stage Grid-connected	Efficiency 97.2%, THD 2.85%, Input current ripple minimized to 0.92A
Boost Converter with Dual Loop Controllers [24]	Two-stage Grid-connected	Efficiency over 95%, Improved frequency nadir by 0.171 Hz, Steady-state frequency increase from 49.812 Hz to 49.841 Hz
Fractional-Order Controller with Boost Converter [25]	1Ø Two-stage Grid-connected	Efficiency 97.5%, THD lower by 0.94%, 1.43%, and 1.86% at 100%, 80%, and 70% capacity, respectively
Semi Z-Source Inverter [26]	Single stage Grid-connected	Efficiency 98%, THD 2.85%, Output voltage stability improved with dynamic response under varying load conditions.
Improved Quasi-Z-Source Converter [27]	Standalone DC-DC converter with resistive load	The efficiency of 94.9%, output voltage 127.3 V from 48 V input, 100 kHz switching frequency
Improved High Voltage Gain Non-Isolated Switched Inductor Quasi Z-Source DC-DC Converter (SIQZSC) [28]	Standalone DC-DC converter with resistive load	Efficiency of 85%, Output voltage 380V from 90V input, 15 kHz switching frequency, Duty ratio: 0.338

Table I presents various DC-DC converter converter topologies and their applications. A thorough review of existing literature on PV systems and DC-DC converter topologies highlights two significant gaps in current research. First, two-stage PV systems typically rely on traditional DC-DC converters such as Boost and SEPIC, as evidenced by studies [14], [16], [19], [24], and [25]. Second, while advanced DC-DC converters, utilizing innovative techniques like VMC, CI, and SC, are extensively employed in standalone DC-DC converter configurations, these advanced techniques are seldom integrated into two-stage GCPV systems. This limits their potential benefits in renewable energy applications, as seen in studies [10], [11], [12], [13], [15], [17], [18], [20], [21], [22], [26], [27], and [28].

To address these gaps, our research makes several important contributions:

1. A new Ćuk converter, combining an SL cell and CI, is integrated into a two-stage, three-phase GCPV system.
2. The impact of the turns ratio in the ĆUK hybrid converter on the system efficiency is explored, revealing its determining influence on the overall performance.
3. Implementing an LCL filter and using a Synchronous Reference Frame Phase Locked Loop (SRF-PLL) to significantly improve power quality and ensure increased grid compliance.
4. Unlike most studies focusing on steady input power conditions, this research evaluates the robustness of PQ control in the DQ framework by simulating dynamic climate conditions.

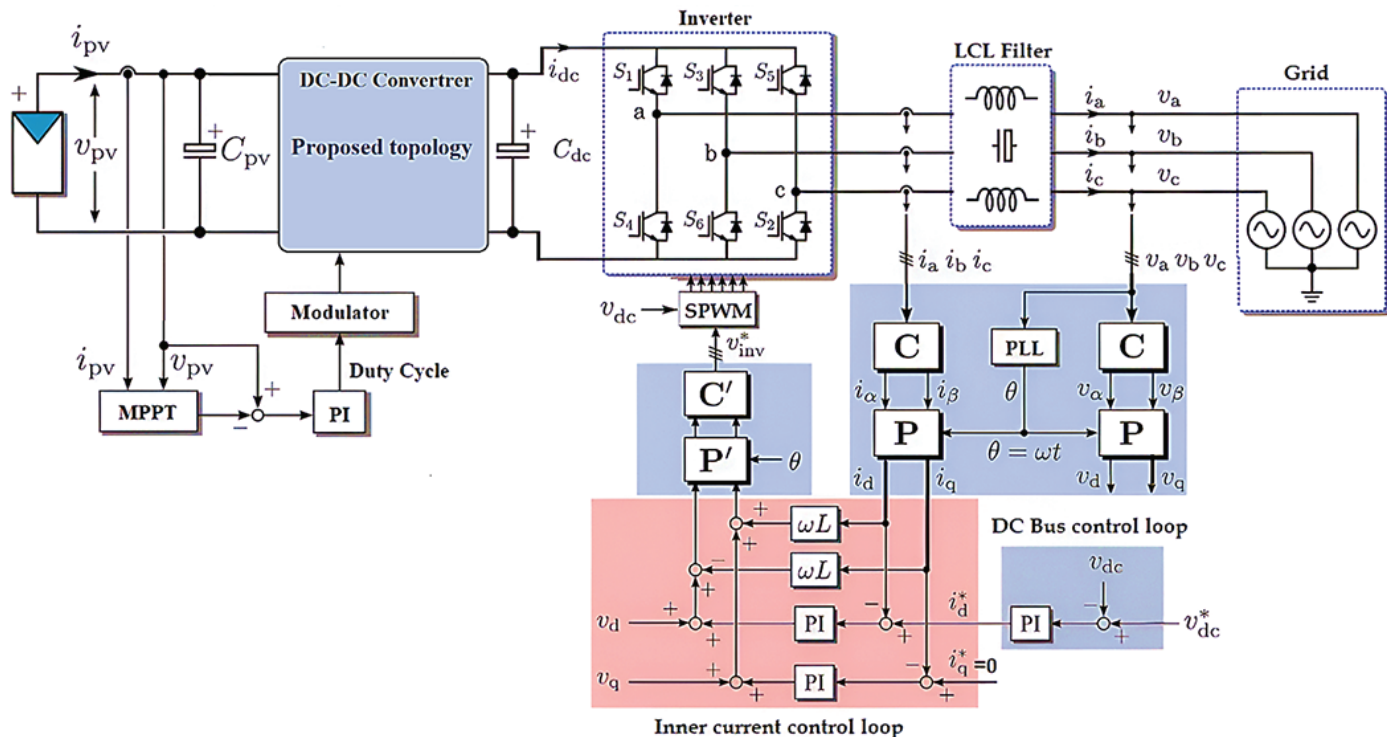


Fig. 1. Double-stage three-phase GCPV system

## II. PROPOSED ADVANCED CONVERTER

This paper is structured to evaluate the performance of a GCPV system utilizing a novel hybrid Ćuk converter. The system architecture begins with PV panels that feed the proposed converter, which is responsible for maximizing power extraction through an MPPT controller. This high-voltage DC output is then converted into AC power. The system's operation is regulated by various control modules, including SRF-PLL [29] for grid synchronization, PQ control in the dq frame for managing active and reactive power [30], and SPWM to ensure a high-quality sinusoidal AC output [31]. The integration of an LCL filter further enhances power quality by reducing high-frequency harmonics [32]. This structure is illustrated in Fig. 1.

The Cuk converter is designed to maintain continuous input and output currents, which reduce the stress on power components [33]. The Cuk converter is also effective in reducing current ripple due to the inductors on both the input and output sides [34]. Additionally, it can invert the output voltage and allow bidirectional power flow, making it useful for applications like renewable energy systems [35].

The operation of the Cuk, as illustrated in Fig. 2(a), is based on two primary modes controlled by the switching of the MOSFET. In Mode 1, when the switch is closed,  $L$  stores energy from the input, and  $C_1$  discharges its energy into the output. Diode D is reverse-biased and does not conduct current.

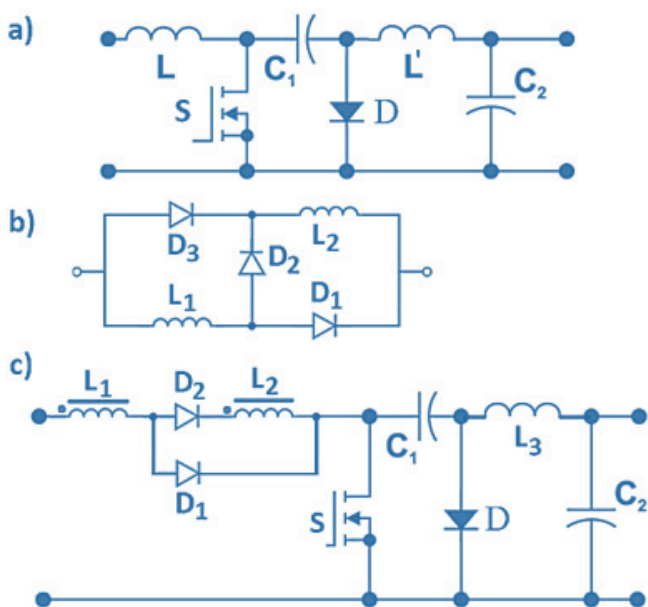


Fig. 2. (a) Conventional Cuk, (b) Switched inductor cell,  
(c) Novel hybrid Cuk

In Mode 2, when the switch is open, the stored energy in  $L$  is transmitted to  $C_1$ , while the diode becomes forward biased, allowing energy to flow to the output side. This two-phase process enables the Ćuk converter to provide a smooth and regulated output with an inverted voltage polarity [36].

In conventional Ćuk converters, achieving high voltage gain often necessitates large duty cycles, which can result in increased losses and reduced efficiency [37]. The introduction of the switched inductor cell, as shown in Fig. 2(b), effectively mitigates this issue by enabling the converter to achieve higher voltage conversion ratios without the need for extreme duty cycles [38]. This cell operates by alternating the charging and discharging of inductors ( $L_1$  and  $L_2$ ), thus multiplying the voltage gain. In Mode 1,  $D_1$  and  $D_3$  conduct, and  $L_1$  and  $L_2$  charge, storing energy. In Mode 2, diodes  $D_1$  and  $D_3$  are turned off while  $D_2$  is conducted, allowing the inductors to discharge their stored energy. This alternating operation efficiently boosts the input voltage and distributes the current and voltage stresses across multiple components. As a result, the overall reliability and lifespan of the converter are enhanced, making it particularly effective for high step-up applications [39].

In the paper [40], a novel hybrid Ćuk converter incorporating both an SL cell and CI is established. During the design of the proposed converter, a critical initial step involved coupling the inductors, designated as  $L_1$  and  $L_2$ , with their respective turn numbers  $N_1$  and  $N_2$ . The purpose of coupling is to improve magnetic energy transfer, reduce current ripple, and increase the static conversion ratio. This setup defines the turns ratio ( $n$ ) as in equation (1) [40].

$$n = \frac{N_2}{N_1} = \sqrt{\frac{L_2}{L_1}} \quad (1)$$

$n$  can be greater than, less than, or equal to one. For the case where the turns ratio  $n$  is greater than 1, diode  $D_3$  remains inactive and can be eliminated from the circuit. This simplifies the topology by reducing the number of components and costs. The resulting converter, as shown in Fig. 2(c), is simpler and more cost-effective. The static conversion ratio, denoted as  $M$ , for the novel Ćuk converter, is provided by equation (2), where  $D$  is the duty cycle, which can be written as equation (3). The coupled inductors ( $L_1$ ,  $L_2$ ) are modeled using the mutual inductance model available in Simulink®. The magnetizing inductance

$L_M$  is determined based on  $L_1$  and  $L_2$  and their coupling coefficient  $k$ , which is set to 0.95. This value is chosen to balance inductor design constraints, ensuring efficient magnetic energy transfer while accounting for inevitable leakage inductance. The equation for calculating the magnetizing inductance  $L_M$  for this mutual inductance model is provided in equation (4).

$$M = -\frac{D}{1-D} \times (1 + n \cdot D) \quad (2)$$

$$D = \frac{-1-M+\sqrt{(1+M)^2+4nM}}{2n} \quad (3)$$

$$L_M = K \sqrt{L_1 \times L_2} \quad (4)$$

$k$  represents the coupling coefficient. The magnetizing inductor current  $I_{LM}$  and output inductor current  $I_{L3}$  are given by:

$$I_{LM} = \frac{D^2(1+n \cdot D)(1+n)}{(1-D)^2} \cdot \frac{V_{PV}}{R} \quad (5)$$

$$I_{L3} = \frac{D(1+n \cdot D)}{1-D} \cdot \frac{V_{PV}}{R} \quad (6)$$

$R$  represents the equivalent load resistance of the grid-connected system as seen by the converter. It is derived based on the power ( $P$ ) of the system and the DC bus voltage ( $V_{dc}$ ) using the formula:  $R = \frac{V_{dc}^2}{P}$ .

The converter also considers small current ripple conditions for the magnetizing inductor and output inductor, ensuring the ripples are less than 25% of the corresponding DC current values. The ripple conditions are expressed as:

$$\Delta I_{LM} = \frac{D \cdot V_{PV}}{L_M f_s} \quad (7)$$

Where  $f_s$  is the switching frequency of the hybrid CUK converter. Furthermore, the voltage and current stresses on the semiconductors are derived to ensure proper design. For the transistor, the voltage stress ( $V_Q$ ) is [40]:

$$V_Q = \frac{1+n \cdot D}{1-D} \cdot V_{PV} \quad (8)$$

And the current stress ( $I_Q$ ) is:

$$I_Q = \frac{D^2(1+n \cdot D)^2}{(1-D)^2} \cdot \frac{V_{PV}}{R} \quad (9)$$

The steady state waveforms are drawn in Fig. 3.

The design of the inductor and capacitance values in the proposed hybrid Ćuk converter is crucial to

ensure optimal performance and low current and voltage ripple. For the inductors, the magnetizing inductor  $L_M$  and the output inductor  $L_3$  are designed based on the small ripple condition, which ensures that the peak-to-peak current ripple does not exceed 25% of the corresponding DC inductor current [40]. The minimum required value of the magnetizing inductor  $L_M$  is expressed as:

$$L_{M-min} = \frac{4}{M \cdot (1+n)} \cdot \frac{R}{f_s \cdot (1-D)} \quad (10)$$

Similarly, the minimum required value for the output inductor  $L_3$  is:

$$L_{3-min} = 4 \cdot (1 - D) \cdot \frac{R}{f_s} \quad (11)$$

These equations ensure that the current ripple through both inductors remains within acceptable limits, enhancing system stability and reducing noise.

The capacitance values are designed to limit the voltage ripple across the internal capacitor  $C_1$  and the output capacitor  $C_2$ . The internal capacitor  $C_1$  is selected based on the condition that the voltage ripple should be less than a predefined percentage (typically 5%) of the DC voltage across the capacitor. The minimum required capacitance is given by:

$$C_{1-min} = \frac{D^2(1+n \cdot D)}{1-D} \cdot \frac{V_{PV}}{\Delta V_{C1} \cdot f_s \cdot R} \quad (12)$$

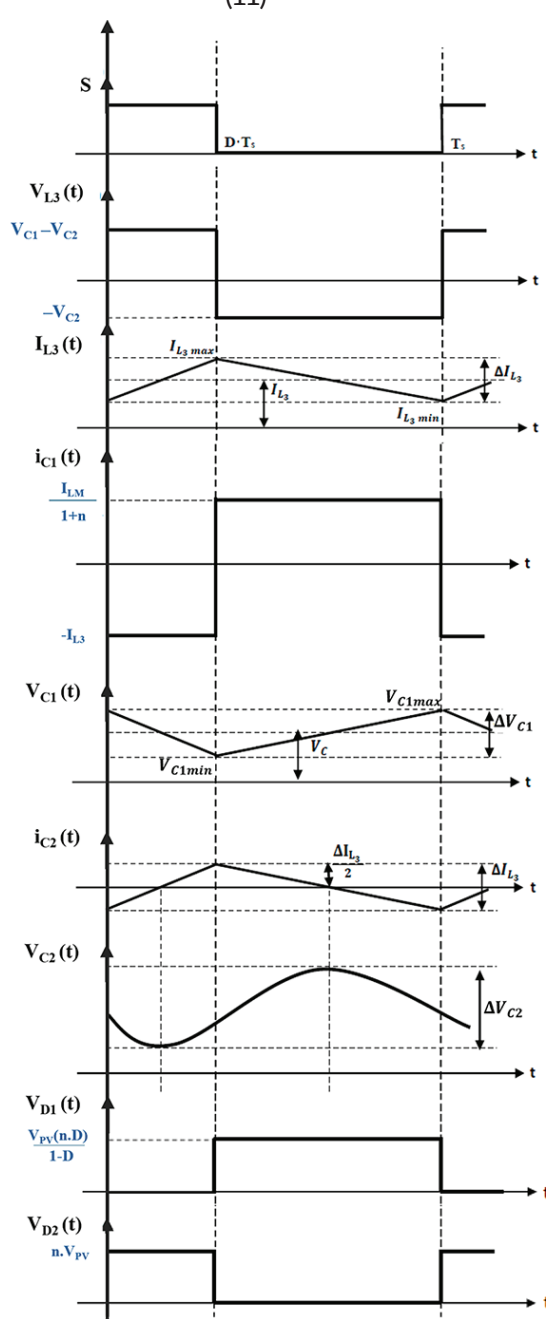


Fig. 3. Main waveforms of the converter

The output capacitor  $C_2$  is essential for stabilizing the converter's output voltage, and its performance is directly affected by the ripple current flowing through it. Higher current ripple leads to increased RMS current, generating heat that can degrade the capacitor's dielectric material and reduce its operational lifespan. To mitigate these effects, the design ensures that the capacitance value of  $C_2$  is selected to limit ripple-induced heating while maintaining voltage stability. Additionally, capacitors with low ESR are preferred to minimize losses. The minimum value of  $C_2$  is calculated as:

$$C_{2-\min} = \frac{1-D}{8 \cdot f_s^2 \cdot L_3} \cdot \frac{V_{C_2}}{\Delta V_{C_2}} \quad (13)$$

### III. AC SIDE CONTROLLER

The system's operation is regulated by various control modules, including SRF-PLL for grid synchronization, PQ control in the dq frame for managing active and reactive power, and Sinusoidal Pulse Width Modulation (SPWM) to ensure a high-quality sinusoidal AC output. The integration of an LCL filter further enhances power quality by reducing high-frequency harmonics. This structure is illustrated in Fig. 1.

#### A. Grid Synchronization with SRF-PLL

The SRF-PLL block in Fig. 4 is responsible for calculating the phase angle, denoted as  $\theta$ , in a way that eliminates the q-component of the voltage ( $v_q$ ) during the conversion from ABC to dq. The ( $v_q$ ) signal is handled by a PI to get the estimated grid's angular frequency  $\omega$ . The frequency is then collected using a voltage-controlled oscillator to determine  $\theta$  [41]. The equation (14) represents the SRF-PLL transfer function, which exhibits a generic second-order system dynamics; the natural frequency ( $\omega_n$ ) and damping factor ( $\zeta$ ) are specified as equation (15) and equation (16), respectively, where  $K_p^{pll}$  and  $K_i^{pll}$  are the proportional and integral gain of the PI controller [41].

$$H_{pll}(s) = \frac{2\xi\omega_n s + \omega_n^2}{s^2 + 2\xi\omega_n s + \omega_n^2} \quad (14)$$

$$\omega_n = \sqrt{K_i^{pll}} \quad (15)$$

$$\xi = \frac{K_p^{pll}}{2\omega_n} = \frac{K_p^{pll}}{2} \sqrt{\frac{1}{K_i^{pll}}} \quad (16)$$

#### B. Current Loop Controller

The current loop controller in Fig. 5 manages the current components along d-axis and q-axis. The control loop includes a PI controller, an inverter transfer function  $H_{inv}(s)$ , and an LCL filter  $H_f(s)$ . The design aims for optimal damping ( $\zeta = 0.7$ ) with proportional and integral gains are determined as in equation (17) [42]:

$$K_p^{id} = \frac{L}{3T_s} \quad \text{and} \quad K_i^{id} = \frac{L}{3T_s T_f} \quad (17)$$

$T_s$  represent the sampling time,  $T_f$  is the filter time constant related to the inductance of LCL filter, and  $L$  represents the total inductance including both inverter-side and grid-side inductances. The detailed design of LCL can be found in [43].

#### C. Voltage Loop Controller

The voltage loop controller in Fig. 6 stabilizes the DC bus voltage by adjusting the current reference. The error between the desired reference voltage ( $V_{DC}^*$ ) and the actual output voltage ( $V_{DC}$ ) is fed into a PI controller, generating the reference current ( $i_d \text{ ref}$ ). The proportional and integral terms parameters  $K_p^v$  and  $K_i^v$  can be designated as in equation (18), where  $C_{DC}$  represents the capacitance of the DC-link, and  $T_{iv}$  is the integrator time constant of the PI controller [42]. The transfer function  $H_v(s)$  describes the relationship between the output d-axis current ( $i_d$ ) and the DC-link voltage ( $V_{DC}$ ) [42]:

$$K_p^v = \frac{C_{DC}}{2\sqrt{T_s T_{iv}}} \quad \text{and} \quad K_i^v = \frac{C_{DC}}{2\sqrt{T_s T_{iv}^3}} \quad (18)$$

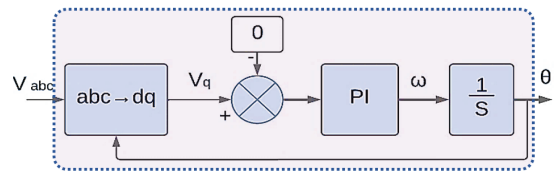


Fig. 4. Three-phase SRF-PLL control loop

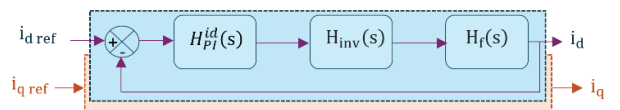


Fig. 5. Current control loop in the synchronous dq frame

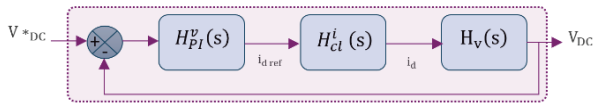


Fig. 6. DC-Bus voltage control loop

## IV. RESULTS AND DISCUSSION

To demonstrate the numerical application of the previously discussed design process, an 8.5 kW grid-connected PV system utilizing the novel hybrid Ćuk converter has been developed. This configuration integrates the proposed converter with an SL cell and CI to power a three-phase inverter. The PV module used in the simulation has a maximum power output of 213.15W. Its open circuit voltage is 36.3V, while the short circuit current reaches 7.84A. At the maximum power point (MPP), the voltage and current are 29V and 7.35A, respectively. The simulation, conducted in the Simulink, explores the impact of various turn ratios on the improved Ćuk converter by assessing their effects on critical parameters such as DC bus voltage ripples, total harmonic distortion (THD), extracted power, and overall system efficiency. Additionally, the performance of the PV system is evaluated Under Varying Irradiance Conditions, focusing on key metrics such as DC bus voltage stability and the quality of the injected current, including THD analysis. Finally, the efficiency of the hybrid Ćuk converter is compared with conventional converters to highlight the advantages of incorporating the switched inductor cell with coupled inductors in the design. Table II outlines the key system parameters for this configuration.

TABLE II. KEY PARAMETERS AND COMPONENTS VALUES

Parameter	Value
Hybrid Ćuk	
Inductor $L_1$	35mH
Inductor $L_2$	7,5mH
Inductor $L_3$	50mH
Capacitor $C_1$	40 $\mu$ F
Capacitor $C_2$	200 $\mu$ F
Capacitor $C_{PV}$	3 $\mu$ F
MPPT Controller	
Switching frequency	10KHz
$K_p$	0,01
$K_i$	0,01
LCL Filter	
$L_{INVERTER}$	6,8mH
C	9 $\mu$ F
$L_{GRID}$	4 mH
Grid	
Voltage (RMS)	380 V
frequency	50 Hz

Inverter controller		
Voltage loop	$K_p^v$	0,13
	$K_i^v$	4
PLL loop	$K_p^{pll}$	1,5
	$K_i^{pll}$	318
Current loop	$K_p^{id} = K_p^{iq}$	72
	$K_i^{id} = K_i^{iq}$	666
Switching frequency		10KHz

### A. Impact of Turns Ratios

The aim of this simulation is to investigate the impact of varying turn ratios on the performance of the hybrid Ćuk converter in a PV system. Specifically, it examines how increasing the turn ratio affects DC bus voltage ripples, total harmonic distortion (THD), and overall power quality. The goal is to determine the optimal turns ratio that provides the best balance between voltage stability, power quality, and system efficiency.

Table III shows that as the turns ratio of the hybrid Ćuk converter increases, both DC bus voltage ripples and THD rise, indicating more voltage fluctuations and slightly reduced power quality. While the extracted power remains nearly constant, it decreases slightly at the highest turns ratio ( $n = 3.5$ ). Efficiency also sees a minor drop from 94% at lower turn ratios ( $n = 1.2$  and  $n = 2$ ) to 93.8% at  $n = 3.5$ . Overall, the best performance in terms of voltage stability, power quality, and efficiency is observed at the lower turns ratio of 1.2. Therefore, for the subsequent simulations, we will use this optimal turn ratio to investigate the system's performance further under Varying Irradiance Conditions.

TABLE III. TURNS RATIO INFLUENCE ON SYSTEM PERFORMANCE

Turns ratio ( $n$ )	$n=1.2$	$n=2$	$n=3.5$
DC bus voltage ripples	0.25%	0.55%	0.78%
THD	1.28%	1.36%	1.68%
Extracted power	8.5KW	8.5KW	8.48KW
Efficiency	94%	94%	93.8%

### B. System Under Varying Irradiance Conditions

Fig. 7 illustrates the irradiance profile used in the simulation, showing fluctuating irradiance levels

between  $1000 \text{ W/m}^2$  and  $200 \text{ W/m}^2$  over 3.5 seconds. These variations reflect dynamic environmental conditions, such as changes in sunlight intensity due to factors like cloud cover. This profile serves to test the PV system's response and stability, particularly in the context of assessing the novel Ćuk converter's ability to maintain stable operation and efficient power transfer despite rapid irradiance changes.

The DC bus voltage response in Fig. 8 demonstrates stable control, with only minor oscillations during the initial period of high irradiance ( $1000 \text{ W/m}^2$ ). Despite the disturbances caused by rapid irradiance drops (to  $400 \text{ W/m}^2$ ,  $600 \text{ W/m}^2$ , and  $200 \text{ W/m}^2$ ), the outer loop voltage control quickly restores the voltage close to the reference level, showcasing effective regulation. As the irradiance increases to  $800 \text{ W/m}^2$ , the voltage remains steady, emphasizing the robustness of the control system in adapting to changing conditions while ensuring system stability. The zoomed-in section highlights minor oscillations that remain well within acceptable limits without causing significant deviations in the voltage.

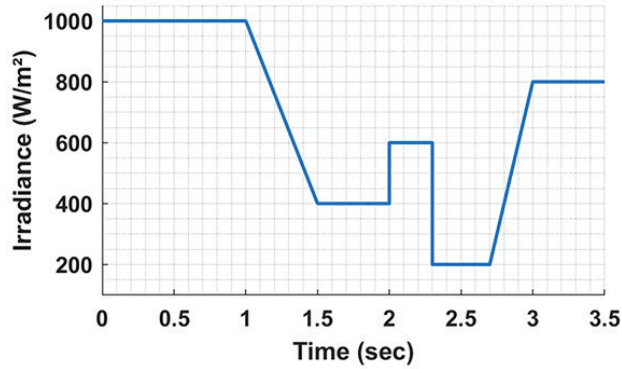


Fig. 7. Irradiance variations

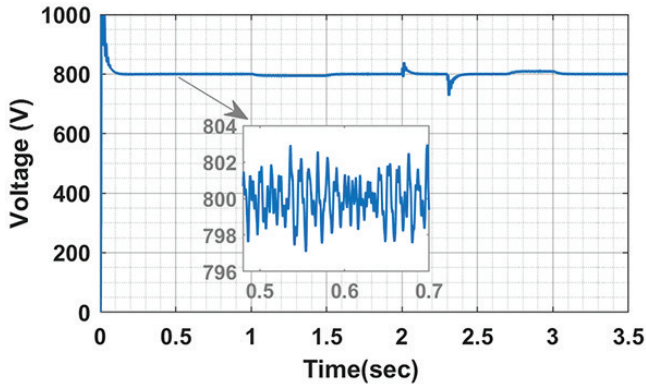


Fig. 8. DC bus voltage

Fig. 9 presents the duty cycle response of the novel hybrid Ćuk converter, which is controlled using a

Perturb and Observe (P&O) MPPT algorithm with a PI controller. The duty cycle adjusts dynamically in response to changing irradiance levels. Initially high during the period of  $1000 \text{ W/m}^2$  irradiance, it decreases as irradiance drops, showing slight disturbances around irradiance shifts at 2 and 2.3 seconds. Despite these fluctuations, the duty cycle stabilizes as irradiance rises to  $800 \text{ W/m}^2$ .

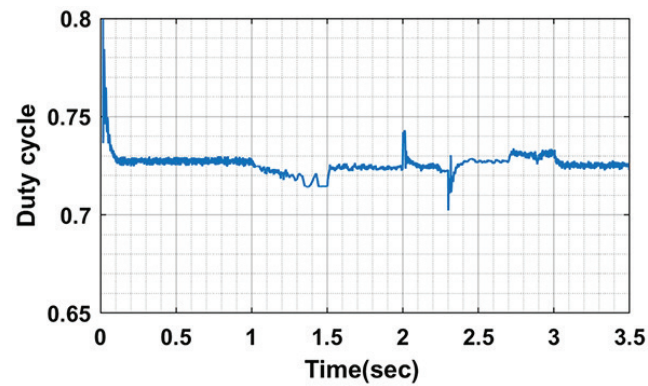


Fig. 9. Proposed converter's duty cycle

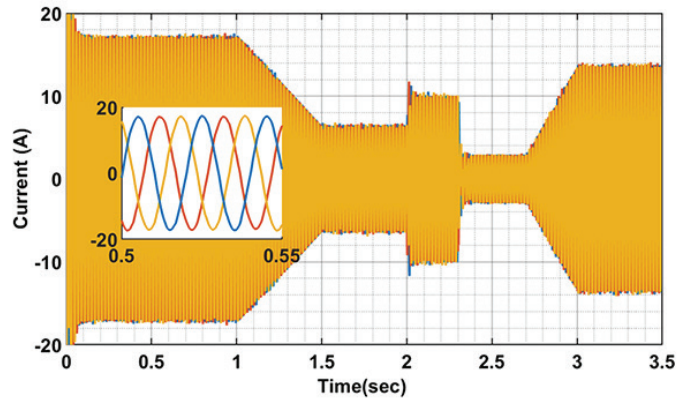


Fig. 10. Grid current

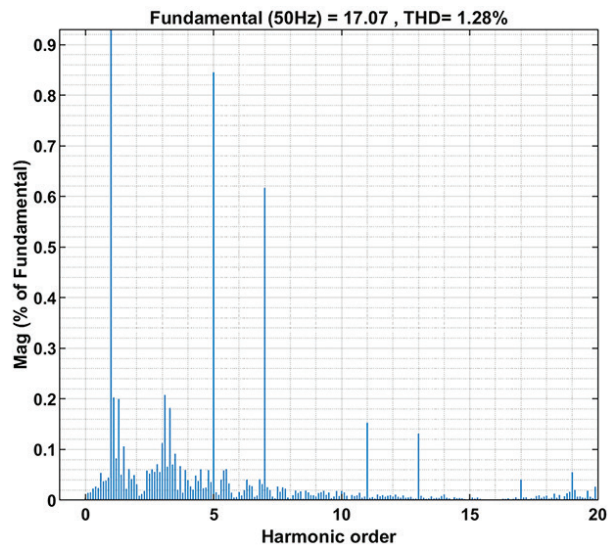


Figure 11. Harmonic current spectrum

Fig. 10 illustrates the injected current into the grid, showing sinusoidal waveforms with variations corresponding to changing irradiance levels. Initially, during high irradiance, the current amplitude reflects a strong power injection into the grid. As irradiance drops to  $400 \text{ W/m}^2$  and further, the amplitude of the current decreases, indicating reduced power output from the PV system. Despite fluctuations in irradiance, the system maintains a consistent waveform, ensuring proper current quality and grid compliance. The accompanying THD analysis in Fig. 11 reveals a low THD of 1.28%. This low THD ensures minimal harmonic interference and compliance with grid standards, reflecting the system's effective operation.

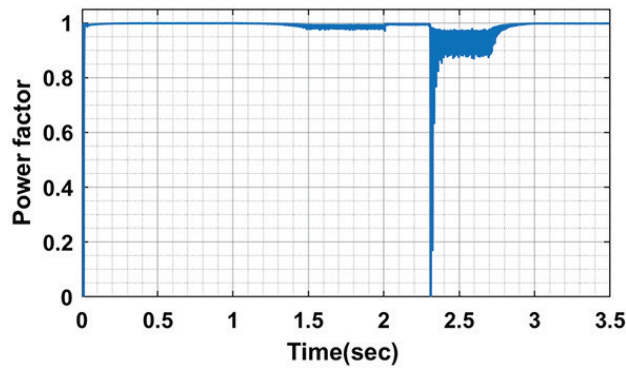


Fig. 12. Power factor of the grid

Fig. 12 shows the power factor response of the system. Initially, the power factor remains close to unity, indicating efficient power transfer with minimal reactive power. However, around the 2.3-second, corresponding to a significant irradiance drop (to  $200 \text{ W/m}^2$ ), the power factor briefly decreases, this drop is short-lived, and the power

factor quickly recovers, returning close to 1.

Fig. 13 illustrates the phase angle variation. The graph shows the phase angle cycling linearly and periodically from 0 to  $2\pi$  radians. This consistent and periodic variation of the phase angle ensures continuous synchronization with the AC grid using SRF-PLL, which is critical for maintaining proper alignment between the inverter output and the grid frequency. This synchronization facilitates efficient power transfer while minimizing phase errors.

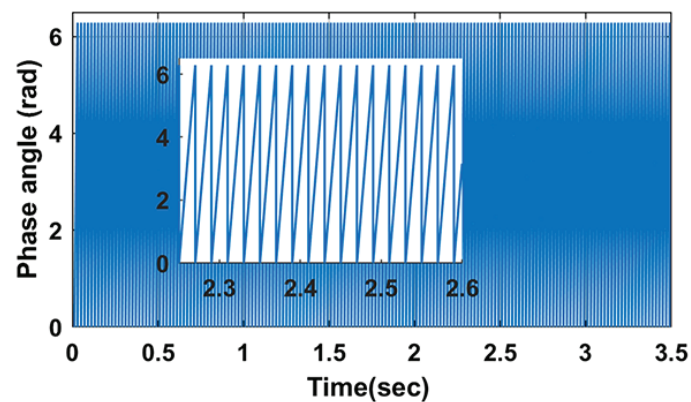


Fig. 13. Phase angle variation

### C. Comparative Efficiency

In this simulation, the efficiency of three DC-DC converters, Hybrid Ćuk, Conventional Ćuk, and Boost, was compared under the same operating conditions, with varying irradiance levels. The objective was to evaluate how each converter performs in terms of efficiency and adaptability to fluctuating solar input.

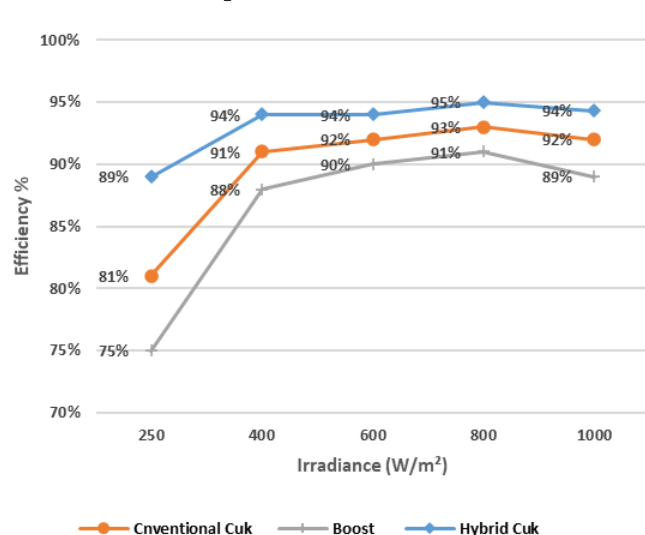


Fig. 14. Efficiency Comparison of Hybrid Ćuk and other Converters

Fig. 14 shows that the Hybrid Cuk converter consistently outperforms the Conventional Cuk and Boost converters in efficiency across varying irradiance levels. The Hybrid converter maintains the highest efficiency, ranging from 89% to 95%, while the Conventional Cuk performs well but slightly lower, with efficiencies between 81% and 93%. The Boost converter has the lowest efficiency, especially at lower irradiance, starting at 75%. Overall, the Hybrid converter is the most efficient and adaptable across different solar conditions.

## V. CONCLUSIONS

In this paper, we proposed and validated a novel hybrid Cuk converter, integrating a switched-coupled inductor cell into a GCPV system. This design addresses the limitations of traditional DC-DC converters. Through simulations conducted in MATLAB/Simulink, the converter demonstrated significant improvements in energy conversion efficiency and power quality, particularly under dynamic climatic conditions. Key findings highlight that the system performs optimally at a lower turns ratio ( $n=1.2$ ), where efficiency reaches 94%, and THD remains low at 1.28%. As the turns ratio increases to  $n=3.5$ , efficiency slightly decreases to 93.8%, and THD rises to 1.68%, indicating a trade-off between voltage gain and power quality. The DC bus voltage

ripples were also minimal, with just 0.25% at  $n=1.2$ , ensuring stable power delivery to the grid. Compared to conventional converters, such as the conventional Cuk and Boost designs, the hybrid Cuk converter consistently maintains higher efficiency across varying solar conditions.

The hybrid Cuk converter offers a more efficient and reliable solution for grid-tied PV systems. Its ability to maintain high efficiency and low THD under dynamic conditions makes it an excellent choice for improving the performance of renewable energy systems, contributing to better energy management and grid stability.

While this study primarily focuses on system-level integration and performance assessment, a critical aspect worth exploring in future research is the detailed optimization of the coupled inductor design. The inductor plays a key role in defining the overall efficiency, bulk, and loss characteristics of the converter. Investigating the trade-offs between coupled and single-winding inductors, considering aspects such as core material selection, magnetic coupling efficiency, thermal behavior, and size reduction, could lead to further improvements in converter performance. Such an analysis would provide valuable insights for practical implementations where space constraints and efficiency are critical factors.

## References

- [1] F. Oufqir, M. Bendaoud, K. Chikh, and A. Lokriti, "Modeling and control of a photovoltaic solar system using a storage and voltage stabilization battery for an efficient microgrid," in *2020 IEEE 2nd International Conference on Electronics, Control, Optimization and Computer Science, ICECOCS 2020*, 2020. doi: 10.1109/ICECOCS50124.2020.9314398.
- [2] F. Oufqir, M. Bendaoud, and K. Chikh, "MPPT-Based a Fuzzy Logic and PO Algorithm for Standalone PV System Under Partial Shading Conditions," in *The Proceedings of the International Conference on Electrical Systems & Automation*, 2022. doi: 10.1007/978-981-9035-8\_1.
- [3] D. Khan, P. Hu, S. Habib, M. Waseem, Z. Lin, and E. M. Ahmed, "A resonant damping control and analysis for LCL-type grid-connected inverter," *Energy Reports*, vol. 8, 2022, doi: 10.1016/j.egyr.2021.11.273.
- [4] M. Bendaoud, F. Oufqir, F. I. Bakhsh, K. Chikh, A. El Fathi, and A. Lokriti, "Comparison and overview of power converter control methods," in *Intelligent Control of Medium and High Power Converters*, 2023. doi: 10.1049/pbpo239e\_ch10.
- [5] P. Kumar and I. Srikanth, "Power quality performance enhancement by PV-based distribution static compensator under incremental conductance maximum power point tracking algorithm," *Cleaner Energy Systems*, vol. 4, 2023, doi: 10.1016/j.cles.2023.100062.
- [6] K. Luo and W. Shi, "Comparison of Voltage Control by Inverters for Improving the PV Penetration in Low Voltage Networks," *IEEE Access*, vol. 8, 2020, doi: 10.1109/ACCESS.2020.3021079.

[7] E. Buraimoh and I. E. Davidson, "Modeling of Double Stage Photovoltaic Inverter System with Fast Delayed Signal Cancellation for Fault Ride-Through Control Application in Microgrids," *Energies (Basel)*, vol. 15, no. 3, 2022, doi: 10.3390/en15030701.

[8] A. Alkhaldi, A. Elkhateb, and D. Laverty, "Voltage Lifting Techniques for Non-Isolated DC/DC Converters," 2023. doi: 10.3390/electronics12030718.

[9] M. K. Nguyen and Y. O. Choi, "Voltage multiplier cell-based quasi-switched boost inverter with low input current ripple," *Electronics (Switzerland)*, vol. 8, no. 2, 2019, doi: 10.3390/electronics8020227.

[10] L. PIANSANGSAN, "A Voltage-Lift Switched Inductor DC/DC Multilevel Boost Converter," *PRZEGŁĄD ELEKTROTECHNICZNY*, vol. 1, no. 4, 2015, doi: 10.15199/48.2015.04.28.

[11] Jude G. M., Pop-Calimanu I. M., and Renken F., "A New Step-Up Converter with Coupled Inductor," in *2020 14th International Symposium on Electronics and Telecommunications*, 2020.

[12] S. Khan *et al.*, "A high step-up DC-DC converter based on the voltage lift technique for renewable energy applications," *Sustainability (Switzerland)*, vol. 13, no. 19, 2021, doi: 10.3390/su131911059.

[13] M. Karthikeyan *et al.*, "A hybridization of cuk and boost converter using single switch with higher voltage gain compatibility," *Energies (Basel)*, vol. 13, no. 9, 2020, doi: 10.3390/en13092312.

[14] S. A. Akbar Fallahzadeh, N. R. Abjadi, A. Kargar, and F. Blaabjerg, "Applying sliding-mode control to a double-stage single-phase grid-connected PV system," *Journal of Renewable Energy and Environment*, vol. 18, no. 1, 2021, doi: 10.30501/JREE.2020.233358.1114.

[15] E. Sreelatha, A. Pandian, P. Sarala, and C. R. Reddy, "Design of Symmetrical Voltage Multiplier High Gain Interleaved DC to DC Converter for Photovoltaic Applications," *Eng. Technol. Appl. Sci. Res.*, vol. 14, no. 3, pp. 14525-14532, 2024.

[16] M.-K. Nguyen and Y.-O. Choi, "Voltage Multiplier Cell-Based Quasi-Switched Boost Inverter with Low Input Current Ripple," *Electronics (Basel)*, vol. 8, no. 2, p. 227, Feb. 2019, doi: 10.3390/electronics8020227.

[17] M. Izadi, A. Mosallanejad, and A. L. Eshkevari, "An improved coupled inductor-based quadratic step-up DC-DC converter with a high step-up factor and reduced voltage overshoot on the power switch," *IET Power Electronics*, vol. 17, no. 9, 2024, doi: 10.1049/pel2.12567.

[18] R. Rahimi, S. Habibi, P. Shamsi, and M. Ferdowsi, "A Dual-Switch Coupled Inductor-Based High Step-Up DC-DC Converter for Photovoltaic-Based Renewable Energy Applications," in *2021 IEEE Texas Power and Energy Conference, TPEC 2021*, 2021. doi: 10.1109/TPEC51183.2021.9384916.

[19] N. Altin, S. Ozdemir, H. Komurcugil, I. Sefa, and S. Biricik, "Two-stage grid-connected inverter for PV systems," in *Proceedings - 2018 IEEE 12th International Conference on Compatibility, Power Electronics and Power Engineering, CPE-POWERENG 2018*, 2018. doi: 10.1109/CPE.2018.8372540.

[20] H. A. K. Hussein and H. J. Motlak, "Improving the design of super-lift Luo converter using hybrid switching capacitor-inductor cell for PV system," *Indonesian Journal of Electrical Engineering and Computer Science*, vol. 25, no. 2, 2022, doi: 10.11591/ijeecs.v25.i2.pp710-720.

[21] S. J. Chen, S. P. Yang, C. M. Huang, and Y. H. Chen, "Interleaved high step-up DC-DC converter with voltage-lift and voltage-stack techniques for photovoltaic systems," *Energies (Basel)*, vol. 13, no. 10, 2020, doi: 10.3390/en13102537.

[22] M. L. Alghaythi, R. M. O'Connell, and N. E. Islam, "Design of a High Step-up DC-DC Power Converter with Voltage Multiplier Cells and Reduced Losses on Semiconductors for Photovoltaic Systems," in *2019 IEEE Electric Ship Technologies Symposium, ESTS 2019*, 2019. doi: 10.1109/ESTS.2019.8847808.

[23] M. W. Lotfy, S. M. Dabour, R. M. Mostafa, D. J. Almakhles, and M. F. Elmorshedy, "Modeling and Control of a Voltage-Lift Cell Split-Source Inverter With MPPT for Photovoltaic Systems," *IEEE Access*, vol. 11, 2023, doi: 10.1109/ACCESS.2023.3280602.

[24] S. Wang, H. Zhu, and S. Zhang, "Two-Stage Grid-Connected Frequency Regulation Control Strategy Based on Photovoltaic Power Prediction," *Sustainability (Switzerland)*, vol. 15, no. 11, 2023, doi: 10.3390/su15118929.

[25] S. Fahad, N. Ullah, A. J. Mahdi, A. Ibeas, and A. Goudarzi, "An advanced two-stage grid connected PV system: A fractional-order controller," *International Journal of Renewable Energy Research*, vol. 9, no. 1, 2019, doi: 10.20508/ijrer.v9i1.9031.g7609.

[26] M. Abdelrahem, M. A. Ismeil, M. Orabi, and R. Kennel, "Three phase semi-Z-source inverter for PV applications," in *PCIM Europe Conference Proceedings*, 2019.

[27] T. Sai, Y. Moon, and Y. Sugimoto, "Improved Quasi-Z-Source High Step-Up DC-DC Converter Based on Voltage-Doubler Topology," *Sensors*, vol. 22, no. 24, 2022, doi: 10.3390/s22249893.

[28] G. Y. Rama Siva Narayana, A. Kumar, and D. C. Das, "Improved high voltage gain non-isolated switched inductor quasi Z-Source DC-DC converter for zero energy DC homes application," in *9th IEEE International Conference on Power Electronics, Drives and Energy Systems, PEDES 2020*, 2020. doi: 10.1109/PEDES49360.2020.9379572.

[29] M. A. Khan, A. Haque, F. Blaabjerg, V. S. B. Kurukuru, and H. Wang, "Intelligent transition control between grid-connected and standalone modes of three-phase grid-integrated distributed generation systems," *Energies (Basel)*, vol. 14, no. 13, 2021, doi: 10.3390/en14133979.

[30] P. K. Gayen, "Novel control approach for enhancing multi-performance of two-stage converter during power transfer from solar photo-voltaic array to AC grid," *Sustainable Energy Technologies and Assessments*, vol. 45, 2021, doi: 10.1016/j.seta.2021.101132.

[31] W. El Maataoui, S. El Daoudi, L. Lazrak, and M. Mabrouki, "Minimized Total Harmonic Distortion of a Multi-level Inverter of a Wind Power Conversion Chain Synchronized to the Grid-LCL Filter Optimization and Third Harmonic Cancellation," *Electrica*, vol. 22, no. 1, 2022, doi: 10.5152/electrica.2021.21086.

[32] C. Srun, P. Chrin, S. Am, and B. Kim, "Modeling and Simulation of a Double-Stage Single-Phase Grid-Connected PV System," *EPI International Journal of Engineering*, vol. 5, no. 1, pp. 16-20, Feb. 2022, doi: 10.25042/epi-ije.022022.03.

[33] S. P. Singh, A. K. Gautam, S. P. Tripathi, and B. Kumar, "Performance comparison of MPPT techniques using Cuk converter for photovoltaic energy conversion system," in *3rd IEEE International Conference on*, 2017. doi: 10.1109/CIAC.2017.7977369.

[34] F. M. TUZTASI, A. B. Yildiz, and H. Kelebek, "Modeling and Analysis of DC-DC CUK Converter with Coupled Inductors," *WSEAS Transactions on Circuits and Systems*, vol. 21, 2022, doi: 10.37394/23201.2022.21.21.

[35] H. Antchev, A. Andonov, and K. Milanov, "Photovoltaic system for LED lighting based on bidirectional Cuk-converter - Computer research," in *2021 17th Conference on Electrical Machines, Drives and Power Systems, ELMA 2021 - Proceedings*, 2021. doi: 10.1109/ELMA52514.2021.9502967.

[36] M. Gupta, N. Gupta, and M. M. Garg, "Performance Analysis of IMC-PID Controller Designed for Cuk Converter with Model Reduction," in *2022 1st International Conference on Sustainable Technology for Power and Energy Systems, STPES 2022*, 2022. doi: 10.1109/STPES54845.2022.10006465.

[37] M. L. Edypoerwa, T. D. Rachmildha, D. Hamdani, D. Mandaris, D. Mandaris, and Yoppy, "Hybrid Modeling and Control of Modified Cuk Converter," in *Proceedings of 2023 4th International Conference on High Voltage Engineering and Power Systems, ICHVEPS 2023*, 2023. doi: 10.1109/ICHVEPS58902.2023.10257520.

[38] P. Sanjeevikumar, P. K. Maroti, F. Blaabjerg, J. B. Holm-Nielsen, D. M. Ionel, and J. He, "Modified CUK Converter with Two Switched Inductor Module Configurations for Photovoltaic Application: Part-II," in *Proceedings - 2020 IEEE International Conference on Environment and Electrical Engineering and 2020 IEEE Industrial and Commercial Power Systems Europe, EEEIC / I and CPS Europe 2020*, 2020. doi: 10.1109/EEEIC/ICPSEurope49358.2020.9160552.

[39] H. Huang, L. Zhang, O. Oghorada, and M. Mao, "Analysis and Control of a Modular Multilevel Cascaded Converter-Based Unified Power Flow Controller," *IEEE Trans Ind Appl*, vol. 57, no. 3, 2021, doi: 10.1109/TIA.2020.3029546.

[40] I. M. Pop-Calimanu, M. Balint, and D. Lascu, "A new hybrid Ćuk DC-DC converter with coupled inductors," *Electronics (Switzerland)*, vol. 9, no. 12, 2020, doi: 10.3390/electronics9122188.

[41] D. Zhou, Y. Song, and F. Blaabjerg, "Modeling and control of three-phase AC/DC converter including phase-locked loop," in *Control of Power Electronic Converters and Systems*, 2018. doi: 10.1016/B978-0-12-805245-7.00005-6.

[42] A. Sangwongwanich, A. Abdelhakim, Y. Yang, and K. Zhou, "Control of single-phase and three-phase DC/AC converters," in *Control of Power Electronic Converters and Systems*, 2018. doi: 10.1016/B978-0-12-805245-7.00006-8.

[43] C. Gurrola-Corral, J. Segundo, M. Esparza, and R. Cruz, "Optimal LCL-filter design method for grid-connected renewable energy sources," *International Journal of Electrical Power and Energy Systems*, vol. 120, 2020, doi: 10.1016/j.ijepes.2020.105998.